



Stabilized *OH species by K^+ -doped Pt for H_2 generation with ultra-low levels of CO through aqueous-phase reforming of methanol at low temperature

You Wang^{a,b,1}, Bing Liu^{c,1}, Qing Guo^a, Yu Sun^a, Sai Zhang^{a,b,*}, Yongquan Qu^{a,**}

^a School of Chemistry and Chemical Engineering, Northwestern Polytechnical University, Xi'an 710072, China

^b Research & Development Institute of Northwestern Polytechnical University in Shenzhen, Shenzhen 518057, China

^c Department of Chemical Engineering, School of Chemical and Material Engineering, Jiangnan University, Wuxi 214122, China

ARTICLE INFO

Keywords:

H_2 generation

Ultra-low levels of CO

Aqueous-phase reforming of methanol

Low temperatures

ABSTRACT

Aqueous-phase reforming of methanol (APRM) represents an attractive approach for H_2 storage and transportation. However, metals with high capacity of methanol activation generally exhibit poor capability for water dissociation and/or weak stabilization of *OH intermediates, leading to the unsatisfactory activity and unavoidable CO generation. Herein, we demonstrated that K^+ -doped Pt nanoparticles on $\gamma-Al_2O_3$ (PtK_x/Al_2O_3) stabilized the *OH intermediates on Pt surface, thereby achieving efficient H_2 generation with ultra-low levels of CO through APRM at 120 °C. Mechanism investigations illustrated that K^+ in Pt nanoparticles shifted the d -band center to stabilize the critical *OH generated from water dissociation without interference on methanol dissociation. Consequently, the PtK_x/Al_2O_3 catalysts delivered a TOF of 142.3 h^{-1} with undetectable CO by gas chromatograph equipped with FID (detection limit: 5 ppm) at 120 °C. These findings are anticipated to promote methanol as a practical H_2 carrier for the delivery of hydrogen with high purity.

1. Introduction

Proton exchange membrane fuel cells (PEMFC) can directly and efficiently convert chemical energy in hydrogen (H_2) into electricity with zero emissions, providing an alternative power supply for a wide range of applications [1–5]. However, one of the limitations of PEMFC is the difficulty in safe storage and convenient transportation of H_2 owing to its low volumetric energy density and high explosibility as well as inflammability [6]. Recently, various liquid organic carriers have been reported as potential approach to achieve safe, convenient, and high-efficiency hydrogen storage system [7–10]. Compared with the other liquid carriers, methanol (CH_3OH) with low freezing point, easy accessibility, low corrosion, and high sustainability has been recognized as an alternative practical hydrogen reservoir [11–13]. Especially, aqueous-phase reforming of methanol (APRM) can release H_2 with a high gravimetric density of 18.8 wt%, which is much higher than other similar organic carriers, such as formic acid (4.5 wt%). Therefore, APRM has been developed as the most attractive and efficient pathway for H_2

storage.

However, the state-of-the-art catalysts generally require high operating temperatures (>200 °C) to guarantee the effective activation of both methanol and water, thereby enabling the efficient H_2 generation through the chemical process of APRM [14–17]. This temperature is far higher than the operation temperatures of PEMFC. Beyond that, the unavoidable CO generation as by-product is detrimental for the direct integration of catalytic APRM system into PEMFC as well as other applications [18–20]. Therefore, developing a qualified catalyst with high activity and ultra-low CO concentration for APRM at low temperatures is highly expected for large-scale and diverse utilization of H_2 energy.

In a typical APRM process, methanol molecule is initially dissociated into *H and *CO along with the generation of two H_2 molecules [12,15,21,22]. Subsequently, the *CO intermediates reform with adjacent *OH species generated from H_2O dissociation, thereafter releasing an additional molecule of H_2 and a molecule of CO_2 [23,24]. Or else, the un-converted *CO intermediates could be released from catalyst surface, leading to the generation of by-product CO [25]. Among various metal

* Corresponding author at: School of Chemistry and Chemical Engineering, Northwestern Polytechnical University, Xi'an 710072, China.

** Corresponding author.

E-mail addresses: zhangsai1112@nwpu.edu.cn (S. Zhang), yongquan@nwpu.edu.cn (Y. Qu).

¹ These authors contributed equally to this work.

catalysts, metallic Pt has been demonstrated as the candidate catalyst owing to its high capacity for methanol dissociation into $^*\text{CO}$ and $^*\text{H}$ [12,26–28]. Unfortunately, similar to other metals [24], the H_2O activation on Pt surface to give the stable $^*\text{OH}$ species is the kinetically limited step for APRM [29–31]. Thus, high operation temperature is still required for Pt-based catalysts. Adding strong bases with high concentrations into the reaction system provides abundant hydroxyls for $^*\text{CO}$ reforming at low temperatures [11,32,33]. However, it induces the serious corrosion issue and reduces the factual H_2 storage capacity of the whole APRM system. A recent key finding is that the interface active sites between atomically dispersed metals and functional supports can achieve H_2 generation via APRM at $< 180^\circ\text{C}$ [12,21]. With the help of functional supports for the efficient activation of H_2O , the interfacial sites generate the abundant and stable $^*\text{OH}$ species for the effective reforming of $^*\text{CO}$ intermediates at low temperatures. However, the H_2 generation with low levels of CO is still not available by these atomically dispersed metal catalysts. On the basis of the recognitions of those systems catalyzed by the metal single-atom catalysts, Pt surrounded by stabilized $^*\text{OH}$ groups with high density is essential to boost both catalytic activity and selectivity of APRM at low temperatures.

Previous reports have proved that the oxidized Pt or other metal oxides can stabilize the $^*\text{OH}$ species to improve the water-gas shift reaction [34,35]. However, the contradiction is that the adsorption and activation of methanol are greatly weakened on the oxidized Pt surface owing to the high coverage of oxygen species [36–38]. Also, the metallic Pt is recognized as a better catalyst for H_2 release [39–41]. Herein, we demonstrated that the introduction of K^+ ions in Pt nanoparticles anchored on the commercial $\gamma\text{-Al}_2\text{O}_3$ support ($\text{PtK}_x/\text{Al}_2\text{O}_3$) broke the contradiction between methanol activation and stability of $^*\text{OH}$ on Pt surface, thereby significantly promoting their catalytic activity for H_2 generation and effectively suppressing the CO generation through APRM process at 120°C . Mechanism investigations suggested that the Pt active sites with the direct interaction of K^+ not only assisted water dissociation but also stabilized the generated $^*\text{OH}$ species to promote the subsequent reforming of $^*\text{CO}$ intermediates. Importantly, due to the charge transfer from potassium to Pt, the capacity of Pt for methanol activation was well preserved. As a result, the $\text{PtK}_x/\text{Al}_2\text{O}_3$ catalysts yielded a high H_2 generation rate with a turnover frequency (TOF) value of 142.3 h^{-1} at 120°C . Most importantly, the level of the generated CO was below the limit of detection of gas chromatograph equipped with FID (5 ppm). This finding is anticipated to benefit the design of highly active and selective catalysts for the sustainable H_2 generation through APRM process at low temperatures.

2. Experimental details

2.1. Preparation of the $\text{PtK}_x/\text{Al}_2\text{O}_3$, $\text{Pt}/\text{Al}_2\text{O}_3$, and $\text{PtSN}/\text{Al}_2\text{O}_3$ catalysts

All three catalysts were prepared by the impregnation method using commercial gamma phase Al_2O_3 (denoted as $\gamma\text{-Al}_2\text{O}_3$) as supports. Briefly, 200 mg of $\gamma\text{-Al}_2\text{O}_3$ was dispersed into 30 mL of ethanol by ultrasonication for 10 min. Then, 0.4 mL of aqueous K_2PtCl_4 solution (Pt: 5.0 mg mL^{-1}) was added to the mixture and stirred for 2 h at room temperature. Subsequently, the solution was slowly evaporated at 90°C . Finally, the dried sample was transferred inside a tube furnace and reduced by a flow of 10 vol% H_2/Ar at 350°C for 2 h to yield the final $\text{PtK}_x/\text{Al}_2\text{O}_3$ catalysts.

The $\text{PtSN}/\text{Al}_2\text{O}_3$ and $\text{Pt}/\text{Al}_2\text{O}_3$ catalysts were prepared by the same method except using $\text{Pt}(\text{NO}_3)_2$ and H_2PtCl_6 as metal precursors instead of K_2PtCl_4 , respectively.

2.2. Preparation of the $\text{Pt-K}_x/\text{Al}_2\text{O}_3\text{-K}_x$ catalysts

As-synthesized $\text{Pt}/\text{Al}_2\text{O}_3$ catalysts after the reduction by 10 vol% H_2/Ar were immediately treated by aqueous KNO_3 solution with various concentrations (K: 0.2 mg mL^{-1} , 0.5 mg mL^{-1} , 1 mg mL^{-1} and 3 mg mL^{-1}). Typically, 1 mL of KNO_3 solution with the desired concentrations was added to 30 mL of ethanol solution with 250 mg of the $\text{Pt}/\text{Al}_2\text{O}_3$ catalysts, which was stirred for 2 h at room temperature. Then, the mixture was evaporated at 90°C . Finally, the dried $\text{Pt-K}_x/\text{Al}_2\text{O}_3\text{-K}_x$ sample was transferred inside a tube furnace and reduced by a flow of 10 vol% H_2/Ar at 350°C for 2 h.

Typically, 1 mL of KNO_3 solution with the desired concentrations was added to 30 mL of ethanol solution with 250 mg of the $\text{Pt}/\text{Al}_2\text{O}_3$ catalysts, which was stirred for 2 h at room temperature. Then, the mixture was evaporated at 90°C . Finally, the dried $\text{Pt-K}_x/\text{Al}_2\text{O}_3\text{-K}_x$ sample was transferred inside a tube furnace and reduced by a flow of 10 vol% H_2/Ar at 350°C for 2 h.

2.3. Preparation of the $\text{Al}_2\text{O}_3\text{-K}_x$ supports and $\text{Pt}/\text{Al}_2\text{O}_3\text{-K}_x$ catalysts

The $\text{Al}_2\text{O}_3\text{-K}_x$ supports were prepared by the impregnation method. Briefly, 1 mL of KNO_3 solution (2 mg mL^{-1}) was added to the 20 mL of ethanol solution with 500 mg of $\gamma\text{-Al}_2\text{O}_3$ supports. After stirring for 2 h at room temperature, the mixture was evaporated at 90°C . Then, the obtained solid was reduced by a flow of 10 vol% H_2/Ar at 350°C for 2 h to yield the $\text{Al}_2\text{O}_3\text{-K}_x$ supports. The $\text{Pt}/\text{Al}_2\text{O}_3\text{-K}_x$ catalysts were prepared by the same impregnation method with $\text{Pt}/\text{Al}_2\text{O}_3$ except using $\text{Al}_2\text{O}_3\text{-K}_x$ as supports instead of the commercial $\gamma\text{-Al}_2\text{O}_3$.

2.4. Catalytic H_2 generation from methanol and H_2O

For a typical catalytic reaction, 50 mg of catalysts were uniformly dispersed in solution with 40 mL of methanol and 18 mL of H_2O by ultrasonic treatment. Then, the mixture was transferred into a 500 mL autoclave equipped with a temperature controller and a pressure detector. Subsequently, the autoclave was purged with N_2 three times, and 1 MPa of N_2 was inflated before catalytic reactions. The temperature of reaction system quickly increased to the given temperature within 10 min. The pressure of autoclave enhanced with the increase of reaction temperatures via real-time monitoring. After reaction, the autoclave was quickly cooled to room temperature by ice bath within 2 min. When the temperature reached room temperature, the gas in the autoclave was collected by a gas sampling bag and analyzed by gas chromatography equipped with TCD and FID. The H_2 was detected by TCD. While CO , CO_2 and CH_4 were detected by FID. The detection limit of FID was 5 ppm.

The H_2 generation rate (r_{H_2}) and TOF value were calculated by Eqs. (1) and (2), respectively.

$$r_{\text{H}_2} = \frac{n_{\text{H}_2}}{m_{\text{cat}} \times t} \quad (1)$$

$$\text{TOF} = \frac{n_{\text{H}_2}}{t \times n_{\text{Pt}} \times D} \quad (2)$$

Where n_{H_2} is the molar mass of generated H_2 ; m_{cat} is the mass of catalysts; t is the reaction time; n_{Pt} and D are the molar mass and dispersion (determined by CO chemisorption) of Pt in the catalysts, respectively.

The selectivity of CO was calculated by Eq. (3):

$$S_{\text{CO}} = \frac{n_{\text{CO}}}{n_{\text{CO}} + n_{\text{H}_2}} \quad (3)$$

Where n_{H_2} and n_{CO} are the molar mass of generated H_2 and CO , respectively.

3. Results and discussion

3.1. Theoretical analysis

Initially, H_2O activation on $\text{Pt}(111)$ surface was investigated by density function theory (DFT) simulation. As shown in Figure 1a and S1a, H_2O molecule adsorbed on $\text{Pt}(111)$ surface with an adsorption energy of -0.45 eV overcomes an energy barrier of 0.91 eV to be dissociated into $^*\text{OH}$ and $^*\text{H}$. However, the relative energy between the initial state and final state is $+0.28\text{ eV}$, suggesting a thermodynamically unfavorable process of H_2O activation on $\text{Pt}(111)$ surface, similar as previous reports [42,43]. More importantly, the $+0.28\text{ eV}$ reaction energy of the formed $^*\text{OH}$ and $^*\text{H}$ intermediates on $\text{Pt}(111)$ surface

strongly indicates their poor thermodynamic stability on Pt, leading to the unsatisfied catalytic performance for APRM. After the introduction of one K atom on Pt(111) surface, the K/Pt(111) shows a stronger interaction with H₂O molecule due to the formation of K-O bond (Fig. S1b), giving a adsorption energy of -0.81 eV. The energy barrier of 0.97 eV is required to enable the H₂O dissociation on the K/Pt(111) surface, which is similar to that on Pt(111) surface. While, the lower reaction energy (-0.19 eV) of *OH and *H formation reveals the thermodynamically favorable process of water dissociation and enhanced thermodynamic stability of *OH species on the K/Pt(111) surface (Fig. 1a and S1b). Considering that K atom is easily oxidized, the K₂O cluster with two K atoms and one O atom is also introduced on Pt(111) surface. On this occasion, H₂O molecule on the K₂O/Pt(111) surface yields the lowest adsorption energy of -0.89 eV (Fig. 1a and S1c), thereby resulting in a most thermodynamically advantageous activation process. Meanwhile, the formed *OH and *H intermediates can be stabilized on the surface of K₂O/Pt(111) with the lowest reaction energy of -0.22 eV (Fig. 1a). To be noted, the energy barrier of water dissociation (0.99 eV) on K₂O/Pt(111) is almost as same as those on K/Pt(111) (0.91 eV) and Pt(111) (0.97 eV), suggesting the unaltered kinetics of water dissociation on three catalysts. Therefore, both K atom and K₂O cluster can thermodynamically improve H₂O dissociation and effectively stabilize the formed *OH intermediate for the subsequent reforming with *CO on Pt(111).

Then, the electronic structures of three Pt surfaces were analyzed to investigate their correlations with methanol activation. As shown in charge density difference results (Fig. 1b), both K atom and K₂O cluster can transfer electrons to adjacent Pt atoms and enhance the electronic density of Pt(111) surface. Specifically, the Bader charge analysis shows one K atom can transfer 0.86 e to the surrounding Pt atoms, giving the charges of 0.13 e, 0.13 e, 0.20 e and 0.19 e to four directly bonded Pt atoms, respectively. Comparatively, the Pt(111) surface receives 0.8 e from the K₂O cluster. The Pt atoms bonded with K atoms accept the

charge of 0.17 e, 0.18 e, 0.13 e and 0.22 e, respectively. Previous reports have proved that the adsorption of methanol is through the interaction between metallic Pt atoms and oxygen atom in methanol for subsequent activation and dissociation [36,38]. The introduction of K or K₂O cluster does not result in the oxidation of Pt(111) surface, thereby maintaining its capacity for methanol activation. To sum up, the DFT calculations predict that the introduction of potassium on Pt surface shows no interference on methanol activation but generates the stabilized *OH intermediate for the promoted reforming of *CO , theoretically boosting the catalytic activity of Pt for APRM at low temperatures.

3.2. Preparation and characterization of catalysts

The PtK_x/Al₂O₃ catalysts were prepared by impregnation methods with K₂PtCl₄ as precursors of both Pt and K and γ -Al₂O₃ as supports. The X-ray diffraction (XRD) patterns showed diffraction peaks of γ -Al₂O₃ (JCPDS 77-0403, Fig. S2), which was well maintained during the synthetic process. The diffraction peaks of Pt were absent in the XRD patterns of as-synthesized catalysts due to the low Pt loading. Transmission electron microscopy (TEM) was utilized to characterize the morphologies and element distributions of the PtK_x/Al₂O₃ catalysts. The dark field TEM images revealed the uniform Pt nanoparticles with an average size of 3.6 ± 0.5 nm on the surface of the γ -Al₂O₃ supports (Fig. 2a and S3). The measured lattice fringe spacing was 0.227 nm, which was consistent with the (111) crystal of metallic Pt (Fig. 2b and c). Determined by the inductively coupled Plasma optical emission spectrometer (ICP-OES) measurement, the actual loadings of Pt and K were 0.99 wt% and 0.45 wt%, respectively (Table 1). Also, the line scanning of the energy dispersive X-ray spectra (EDX) of Pt nanoparticles exhibited the similar distributions of K element with Pt element, strongly confirming that the K element was mainly distributed on the Pt nanoparticles rather than the surface of γ -Al₂O₃ supports (Fig. 2d).

Parallely, the Pt nanoparticles supported on the γ -Al₂O₃ supports with H₂PtCl₆ or Pt(NO₃)₂ as precursors were prepared by the identical impregnation to explore the possible influence of K element on the catalytic performance of Pt for H₂ generation. When H₂PtCl₆ was selected as metal precursors to yield the Pt/Al₂O₃ catalysts, the Pt nanoparticles with the size of 3.9 ± 0.5 nm on the surface of Al₂O₃ supports was observed from dark field TEM images (Fig. S4a and S4b). The lattice fringe spacing of 0.224 nm confirmed the metallic state of Pt nanoparticles in Pt/Al₂O₃ (Fig. S4c and S4d). The actual Pt loading in Pt/Al₂O₃ was 1.05 wt% (Table 1). While, no K element was detected from the ICP-OES measurements. Assuming that the ratio of a CO to surface Pt atom is $1:1$ [44,45], the dispersion of Pt nanoparticles in Pt/Al₂O₃ was 16.7% by calculating the $n(\text{CO}_{\text{chemisorbed}})/n(\text{Pt}_{\text{total}})$ ratio, which was similar with the Pt dispersion in PtK_x/Al₂O₃ (19.3%). Meanwhile, the Al₂O₃ supported relatively small Pt nanoparticles (PtSN/Al₂O₃) with an average size of 1.8 ± 0.2 nm (Fig. S5a and S5b) and an actual Pt loading of 0.86 wt% were prepared by using Pt(NO₃)₂ as metal precursors. The dispersion of Pt was as high as 31.8% for the PtSN/Al₂O₃ catalysts. Also, the lattice fringe spacing of small Pt nanoparticles was 0.222 nm (Fig. S5c and S5d), also suggesting the metallic state of Pt in the PtSN/Al₂O₃ catalysts.

Then, the surface chemical status of various catalysts was analyzed by X-ray photoelectron spectroscopy (XPS). As shown in Fig. 2e, compared with Pt/Al₂O₃ and PtSN/Al₂O₃, only the PtK_x/Al₂O₃ catalysts exhibited the K $2p$ peak at 293.1 eV (K $2p_{3/2}$) and 295.9 eV (K $2p_{1/2}$), revealing the presence of the oxidized potassium species. Taking the ICP-OES, EDS mapping and XPS results into accounts, the K⁺ doped Pt nanoparticles were experimentally illustrated in the PtK_x/Al₂O₃ catalysts. The binding energy of Pt $4d_{5/2}$ for PtK_x/Al₂O₃ was 314.3 eV, which was slightly lower than the binding energy of 314.7 eV for Pt/Al₂O₃ and PtSN/Al₂O₃ (Fig. 2f). Therefore, the electron density of Pt nanoparticles was increased after K⁺ doping, consistent with the DFT simulations.

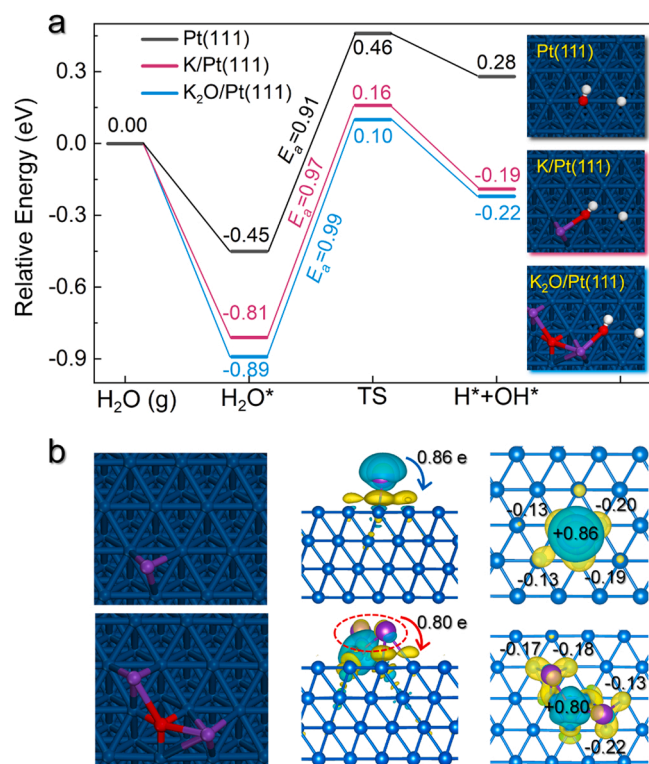


Fig. 1. (a) Adsorption and dissociation of H₂O on Pt(111), K/Pt(111) and K₂O/Pt(111) surfaces. (b) Charge density difference and Bader charge analysis of K/Pt(111) and K₂O/Pt(111). Blue and yellow isosurfaces represent electron depletion and accumulation, respectively.

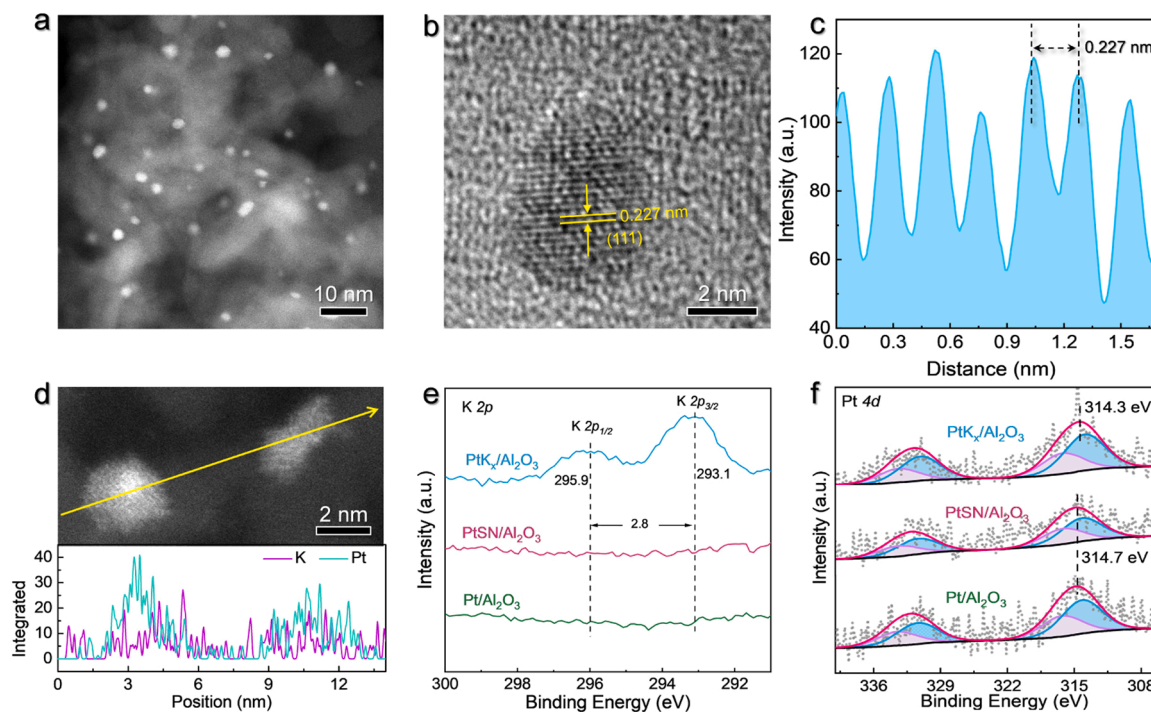


Fig. 2. (a) Dark field TEM image and (b) High resolution TEM image of the $\text{PtK}_x/\text{Al}_2\text{O}_3$ catalysts. (c) The intensity profiles of Pt crystal plane spacing. (d) HAADF-STEM image and EDX line spectra along the yellow arrow. XPS analysis of (e) K 2p and (f) Pt 4d peaks of various Pt-based catalysts.

Table 1

Physical structure parameters of different catalysts.

Entry	Catalysts	Metal content (wt%) ^a		Average size of Pt (nm) ^b	Dispersion of Pt (%) ^c
		Pt	K		
1	$\text{PtK}_x/\text{Al}_2\text{O}_3$	0.99	0.45	3.6 ± 0.5	19.3
2	$\text{Pt}/\text{Al}_2\text{O}_3$	1.05	-	3.9 ± 0.5	16.7
3	$\text{PtSN}/\text{Al}_2\text{O}_3$	0.86	-	1.8 ± 0.3	31.8
4	$\text{PtK}_x/\text{Al}_2\text{O}_3\text{-K}_x$	1.06	0.40	3.0 ± 0.4	27.2
5	$\text{Pt}/\text{Al}_2\text{O}_3\text{-K}_x$	1.01	0.40	3.1 ± 0.4	26.5

^a Measured by ICP-OES.

^b At least 200 Pt particles were calculated from dark-field TEM images.

^c Determined by CO chemisorption.

3.3. Catalytic performance of H_2 generation

The H_2 generation through APRM process was performed with n (CH_3OH): n (H_2O) of 1:1 in the absence of bases and other additives. The total mass of catalysts and N_2 pressure were controlled at 50 mg and 1 MPa, respectively. At 120 °C, no H_2 was detected from the APRM catalyzed by $\text{Pt}/\text{Al}_2\text{O}_3$. Reducing the size of Pt nanoparticles could improve the catalytic performance of APRM and lead to a H_2 generation rate of $290.2 \mu\text{mol g}_{\text{cat}}^{-1} \text{h}^{-1}$ for the $\text{PtSN}/\text{Al}_2\text{O}_3$ catalysts under the identical reaction conditions. Comparatively, the H_2 generation rate of $\text{PtK}_x/\text{Al}_2\text{O}_3$ was significantly promoted to $1379.5 \mu\text{mol g}_{\text{cat}}^{-1} \text{h}^{-1}$, which was 4.7 times higher than that of $\text{PtSN}/\text{Al}_2\text{O}_3$ (Fig. 3a). In order to explore their intrinsic catalytic activity, the TOF value of H_2 generation for $\text{PtK}_x/\text{Al}_2\text{O}_3$ was 142.3 h^{-1} , which was 6.4 times higher than that (22.1 h^{-1}) of $\text{PtSN}/\text{Al}_2\text{O}_3$ (Fig. 3b). Such a significantly enhanced TOF of H_2 generation by $\text{PtK}_x/\text{Al}_2\text{O}_3$ was comparable to those systems catalyzed by the representative noble metal-based homogeneous catalysts at similar reaction temperatures, as shown in Table S1 [32,33,46–48].

Then, the kinetic study was performed for $\text{PtK}_x/\text{Al}_2\text{O}_3$ and $\text{PtSN}/\text{Al}_2\text{O}_3$ to probe the influence of K^+ ions on Pt catalyzed H_2 generation from APRM reaction. It was found that the accumulated H_2 production almost increased linearly with the reaction time during the initial 4 h

(Fig. S6a). Also, the H_2 generation rates at various reaction times were almost constant in the range of $1284.3 \mu\text{mol g}_{\text{cat}}^{-1} \text{h}^{-1}$ and $1377.5 \mu\text{mol g}_{\text{cat}}^{-1} \text{h}^{-1}$ (Fig. S6b). It suggested a zero-order reaction of APRM catalyzed by $\text{PtK}_x/\text{Al}_2\text{O}_3$ for H_2 generation during the initial period due to the excessive amount of reactant and low conversions of methanol. Also, the feature of external diffusion limitation free for zero-order reaction could be further confirmed from the barely influenced H_2 generation rates under different stirring speeds (Fig. S7). As a result, the reaction rates were easily determined by the generated amount of H_2 during unit time. When the reaction temperatures raised from 120 °C to 150 °C, both $\text{PtK}_x/\text{Al}_2\text{O}_3$ and $\text{PtSN}/\text{Al}_2\text{O}_3$ delivered the improvement of H_2 generation. Similar to the catalytic activity at 120 °C, the H_2 generation rate of $\text{PtK}_x/\text{Al}_2\text{O}_3$ was invariably higher than that of $\text{PtSN}/\text{Al}_2\text{O}_3$ at each temperature (Fig. S8). The derived value of activation energy (E_a) of $\text{PtK}_x/\text{Al}_2\text{O}_3$ for APRM was 74.8 kJ mol^{-1} , which was 1.4 times lower than that of $\text{PtSN}/\text{Al}_2\text{O}_3$ ($104.8 \text{ kJ mol}^{-1}$, Fig. 3c and d). Therefore, the low activation energy (E_a) also revealed the high capacity of $\text{PtK}_x/\text{Al}_2\text{O}_3$ for APRM. The doping of K^+ in Pt nanoparticles significantly enhanced their catalytic activity for H_2 generation through APRM at low temperatures.

Another encouragement was that the $\text{PtK}_x/\text{Al}_2\text{O}_3$ catalysts also exhibited remarkable capability to suppress CO generation. When $\text{PtK}_x/\text{Al}_2\text{O}_3$ was used as catalysts for APRM, the by-product of CO was not detected by the gas chromatography (GC) at 120 °C during the H_2 generation process. In contrast, the $\text{PtSN}/\text{Al}_2\text{O}_3$ catalysts yielded a CO selectivity of 0.045% even at a low H_2 generation rate (Fig. 3b). In addition, the $\text{PtK}_x/\text{Al}_2\text{O}_3$ catalysts also exhibited satisfactory stability for the APRM in the absence of any base and additives. After each cycle, the $\text{PtK}_x/\text{Al}_2\text{O}_3$ catalysts were collected by centrifugal separation and reused for the next cycle without extra treatment. As shown in Fig. 3e, the TOF values of $\text{PtK}_x/\text{Al}_2\text{O}_3$ for H_2 generation were well maintained in the range of 149.8 h^{-1} to 122.3 h^{-1} at least for 8 cycles. Importantly, no CO by-product was detected by GC during the stability testing. Both size and electronic structure of Pt nanoparticles for the spent $\text{PtK}_x/\text{Al}_2\text{O}_3$ catalysts (Fig. S9a-S9c) showed the bare changes in comparison with those of as-synthesized $\text{PtK}_x/\text{Al}_2\text{O}_3$ catalysts. Compared with as-

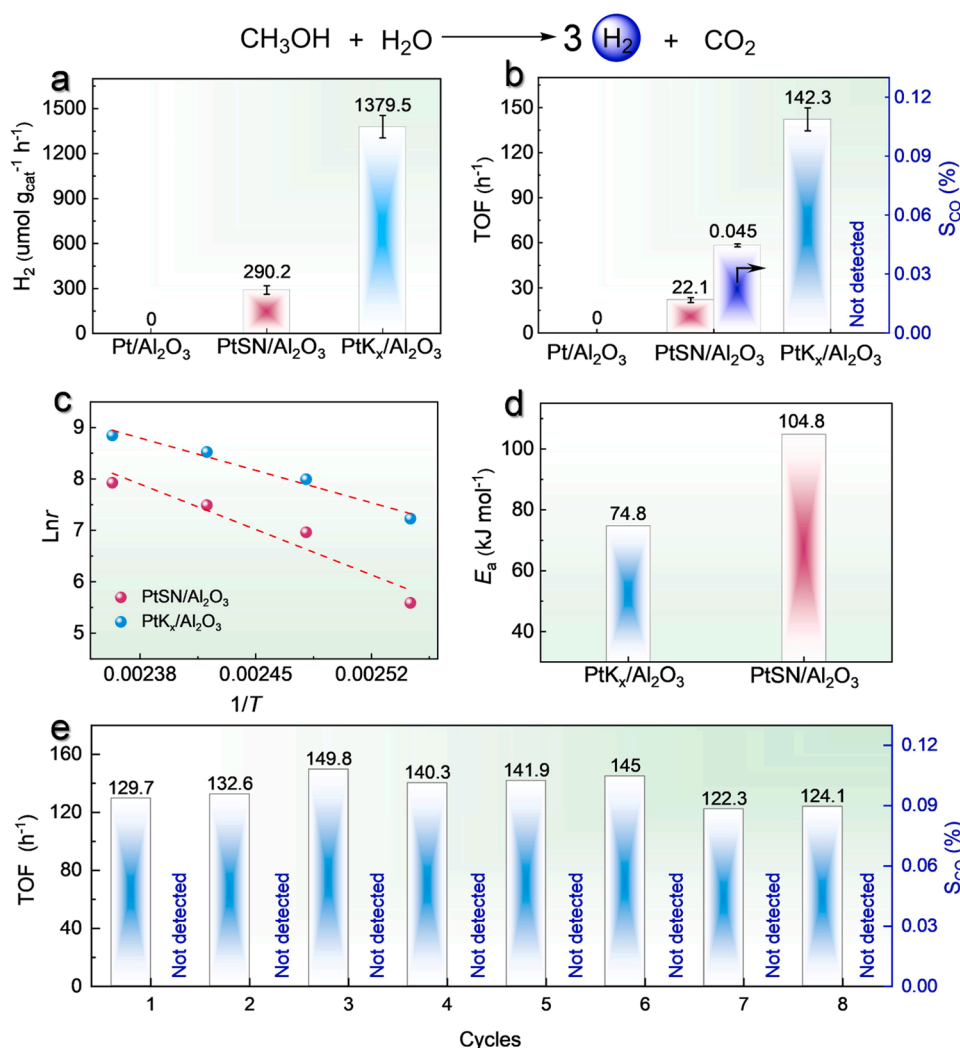


Fig. 3. (a) H₂ generation rates, (b) calculated TOF values and CO selectivities of various Pt-based catalysts. **Reaction conditions:** catalysts (50 mg), CH₃OH (40 mL), H₂O (18 mL), 120 °C, N₂ (1.0 MPa) and 2 h. (c) Lnr, derived from H₂ generation rates *versus* reaction times, as a function of 1/T for various Pt-based catalysts. (d) The derived values of activation energy of various catalysts for H₂ generation. (e) Cycling performance and CO selectivities of PtK_x/Al₂O₃ for H₂ generation via APRM. **Reaction conditions:** catalysts (50 mg), CH₃OH (40 mL), H₂O (18 mL), 120 °C and N₂ (1.0 MPa). The reaction time for each cycle was 2 h.

synthesized PtK_x/Al₂O₃ catalysts, the K content in the spent PtK_x/Al₂O₃ catalysts decreased from 0.45 wt% to 0.36 wt% after the firstly cycling test. The initial loss of K⁺ could be attributed to the dissolution of the physically adsorbed K⁺ on the catalyst surface. However, after the eighth cycles, 0.31 wt% of K content was still preserved on the spent PtK_x/Al₂O₃. The K 2p peak was also detected from XPS analysis, suggesting the presence of K element in the spent PtK_x/Al₂O₃ catalysts after eighth cycles. More importantly, the influence of K element on the electronic structure of Pt nanoparticles was still maintained because the binding energy of Pt 4d peak was not changed (Fig. S9c and S9d). Thus, the chemically bonded K⁺ on the surface of catalysts could be stabilized during H₂ generation process. The maintained catalytic performance and the preserved structure confirmed the catalytic stability of PtK_x/Al₂O₃ for H₂ generation through APRM process. Therefore, such low CO selectivity and satisfactory H₂ generation rate as well as good stability of the PtK_x/Al₂O₃ catalysts exhibited their great potentials to fulfill the practical demands for H₂ generation with high purity at low temperatures.

3.4. Mechanism

Based on the comparative catalytic performance, the PtK_x/Al₂O₃ catalysts yielded the satisfactory H₂ generation rate with ultra-low levels of CO at a low temperature of 120 °C, which had not been achieved for the APRM by the reference catalysts (Pt/Al₂O₃ and PtSN/Al₂O₃) or previous reports (Table S1). For the typical Pt catalysts, the *CO

intermediates generated from CH₃OH dissociation are strongly adsorbed on Pt surface. When Pt surface is lack of the *OH intermediates (Fig. 1a), the reforming of *CO intermediate is unsatisfactory (Fig. 4a), further leading to the slow recycle of Pt active sites at low temperatures. It makes sense to observe the bare activity of the Pt/Al₂O₃ catalysts for H₂ generation at 120 °C. Different from the previously reported facilitation by functional supports [12,15,21,22], our DFT analysis revealed that the presence of K⁺ in Pt nanoparticles provided a novel approach to stabilize the critical *OH intermediates for the subsequent reforming of *CO (Fig. 4b), boosting the H₂ generation and avoiding the CO release. Therefore, control experiments were further performed to supplement the DFT results and reveal the catalytic mechanism.

Initially, the critical roles of H₂O molecule in H₂ generation via APRM were explored. Under the same conditions, PtK_x/Al₂O₃ was used to catalyze the H₂ generation from methanol in the absence of H₂O. The H₂ generation rate was only 101.3 μmol g_{cat}⁻¹ h⁻¹, which was obviously lower than the rate from methanol and H₂O system (Fig. S10a). Due to the lack of H₂O, the reforming of adsorbed *CO intermediates was not occurred. As a result, a large amount of CO was released from the methanol system (Fig. S10b). Obviously, the absence of H₂O could directly reduce the H₂ generation rate with the inevitable generation of CO.

Then, the presence of K⁺ for the improvement of H₂ generation from methanol and H₂O were further confirmed. Considering no catalytic activity of Pt/Al₂O₃ for APRM, the as-synthesized catalysts were further treated by aqueous KNO₃ solution with various concentrations to

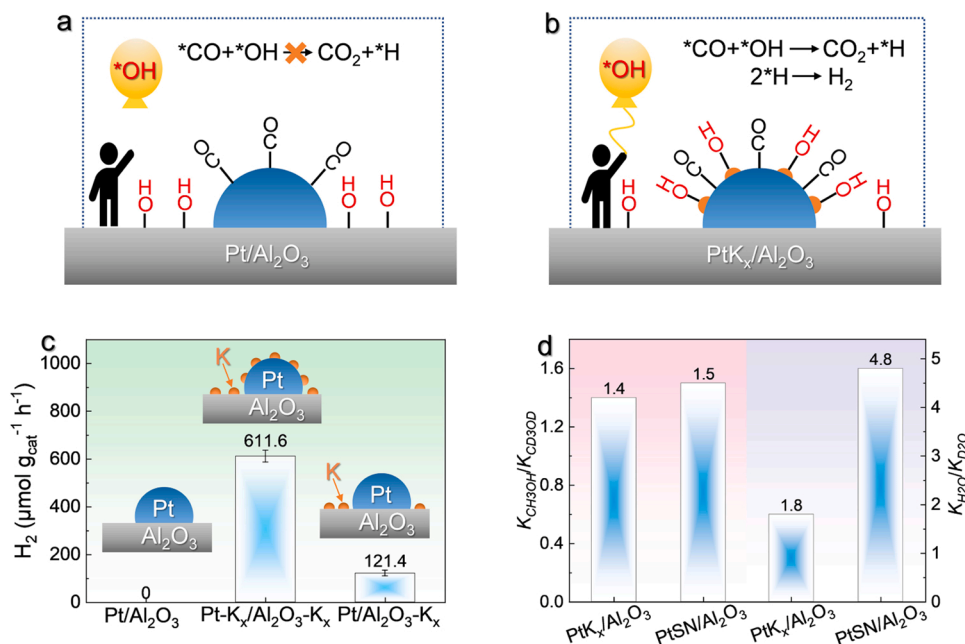


Fig. 4. The scheme of reforming of *CO intermediate on (a) Pt/Al_2O_3 and (b) PtK_x/Al_2O_3 . **Note:** The balloon with rope represents the *OH intermediates. While the man represents the Pt active sites. (c) H_2 generation rates of the Pt/Al_2O_3 , $PtK_x/Al_2O_3-K_x$ and $Pt/Al_2O_3-K_x$ catalysts. (d) Isotope experiments. Ratios of H_2 generation rates from CH_3OH/H_2O to CD_3OD/H_2O as well as the ratios of H_2 generation rates from CH_3OH/H_2O to CH_3OH/D_2O . **Note:** the by-product of CO was not detected by GC in Figs. 3d and 4d. **Reaction conditions:** catalysts (50 mg), CH_3OH/CD_3OD (40 mL), H_2O/D_2O (18 mL), $120\ ^\circ C$, N_2 (1.0 MPa) and 2 h.

introduce K^+ on both the surface of Pt nanoparticles and Al_2O_3 support (Fig. S11). The KNO_3 -treated Pt/Al_2O_3 catalysts were named as $PtK_x/Al_2O_3-K_x$. The H_2 generation rates of various $PtK_x/Al_2O_3-K_x$ catalysts increased initially and then decreased with the increased K^+ loadings at $120\ ^\circ C$ (Fig. S12). The highest rate of $611.6\ \mu mol\ g_{cat}^{-1}\ h^{-1}$ for $PtK_x/Al_2O_3-K_x$ was yielded with a K^+ loading of 0.4 wt% (Fig. 4c). More importantly, the release of CO was effectively curbed when the K^+ loading was higher than 0.2 wt% (Fig. S12). Due to no catalytic activity of Pt/Al_2O_3 for APRM at $120\ ^\circ C$, the boosted performance of $PtK_x/Al_2O_3-K_x$ was definitely attributed to the presence of K^+ .

Subsequently, the importance of the direct contact between K^+ and Pt was further evaluated for H_2 production from methanol and H_2O . The commercial Al_2O_3 supports were treated by KNO_3 to obtain the K^+ modified supports of $Al_2O_3-K_x$. Under the same reaction conditions, there was no H_2 generation by $Al_2O_3-K_x$, revealing the natural catalytic capacity of Pt (Fig. S13). Afterwards, the Pt nanoparticles supported on $Al_2O_3-K_x$ ($Pt/Al_2O_3-K_x$) were prepared by the same impregnation process of Pt/Al_2O_3 (Fig. S14). Thus, only the Pt atoms at the $Pt/Al_2O_3-K_x$ interface exhibited the possibility to directly contact with K^+ . Under the same reaction conditions, the $Pt/Al_2O_3-K_x$ catalysts yielded a H_2 generation rate of only $121.4\ \mu mol\ g_{cat}^{-1}\ h^{-1}$, which was 5.0 times lower than that of $PtK_x/Al_2O_3-K_x$ ($611.6\ \mu mol\ g_{cat}^{-1}\ h^{-1}$, Fig. 4c). Therefore, the significantly low H_2 generation rate of $Pt/Al_2O_3-K_x$ further indicated the improvement of K^+ for APRM via its direct interaction with Pt .

Next, the H/D isotope experiments were performed on the $PtSN/Al_2O_3$ and PtK_x/Al_2O_3 catalysts at $120\ ^\circ C$ to demonstrate the influences of K^+ on the activation of H_2O or CH_3OH . Derived from their H_2 generation rates via APRM, for the $PtSN/Al_2O_3$ catalysts, the values of k_{CH_3OH}/k_{CD_3OD} and k_{H_2O}/k_{D_2O} were 1.5 and 4.8, respectively (Fig. 4d), revealing that the H_2O activation was the rate-determining step of the $PtSN/Al_2O_3$ catalysts. For the PtK_x/Al_2O_3 catalysts, the value of k_{CH_3OH}/k_{CD_3OD} was 1.4, which was similar to the value of $PtSN/Al_2O_3$ (1.5). Those two close values suggested the bare influences of K^+ ions on Pt nanoparticles for the methanol activation herein, consistent with the DFT calculations. It was noted that the value of k_{H_2O}/k_{D_2O} for PtK_x/Al_2O_3 was dramatically reduced to 1.8, which was significantly lower than that for $PtSN/Al_2O_3$ (Fig. 4d). Therefore, the presence K^+ could effectively enhance the dissociation of H_2O to generate the stabilized *OH on Pt surface, thereby promoting the H_2 generation through APRM reaction via the accelerated reforming of *CO .

Subsequently, the *in-situ* diffuse reflectance infrared Fourier transform spectroscopy (DRIFTS) measurements were carried out to further investigate the stabilization of *OH . In order to exclude the interference of hydroxyl of Al_2O_3 supports on the characteristic infrared peaks of *OH , the K_2PtCl_4 and H_2PtCl_6 metal precursors were directly calcined in the 10 vol% H_2/Ar to yield the PtK_x and Pt nanoparticles, respectively. The obtained Pt and PtK_x nanoparticles were further treated by H_2O at $120\ ^\circ C$. The obtained Pt/PtK_x nanoparticles were purged under Ar at atmosphere at $20\ ^\circ C$ to remove the physically adsorbed H_2O molecules. As shown in Figs. 5a and 5b, both PtK_x and Pt surfaces exhibited the weak characteristic peak of $-OH$ at $\sim 3720\ cm^{-1}$. Meanwhile, the obvious peaks of $H-O-H$ at about $1660\ cm^{-1}$ were observed from *in-situ* DRIFTS [49–51]. When the temperature was gradually elevated to $50\ ^\circ C$, $100\ ^\circ C$ and $150\ ^\circ C$, the characteristic peaks of $H-O-H$ exhibited the similar reduction on PtK_x and Pt surface, revealing the similar consumption and dissociation behavior of H_2O molecules. Importantly, the increasing rate of $-OH$ peak on PtK_x surface was significantly higher than that on Pt surface, suggesting the weaker stabilization of the generated *OH intermediates on Pt surface. When the temperature was maintained at $150\ ^\circ C$, the peak intensity of $-OH$ on PtK_x surface remained almost constant (Fig. 5c). In contrast, the $-OH$ on Pt surface reduced obviously to deliver an apparent drop in peak intensity (Fig. 5d). The difference in $-OH$ intensity of PtK_x and Pt directly indicated the stronger stabilization of *OH intermediates on PtK_x surface than on Pt surface. Therefore, the *in-situ* DRIFTS results distinctly illustrated the enhanced stabilization of *OH intermediates for the K^+ ions doped Pt nanoparticles, thereby promoting the H_2 generation through APRM at low temperatures.

In addition, the *d*-band electron structures of various catalysts were characterized by the high-resolution valence-band XPS spectra to experimentally explore the essential cause of the stabilized *OH intermediate on Pt surface. According to the *d*-band center theory [52–54], when a transition metal surface is chemically adsorbed with a small molecule, the *d*-band of metal will hybridize with an induced state of molecule to form fully filled bonding and partially filled antibonding states. When the *d*-band center is shifted up relative to the Fermi level, the low filling degree of antibonding states further results in the strong bonding of adsorbates. Compared with the Pt/Al_2O_3 and $PtSN/Al_2O_3$ catalysts, the presence of K^+ ions led to a significant shift of *d*-band center towards the valence band maximum (VBM) of the PtK_x/Al_2O_3 catalysts (Fig. S15), thereby resulting in the strong interaction with *OH .

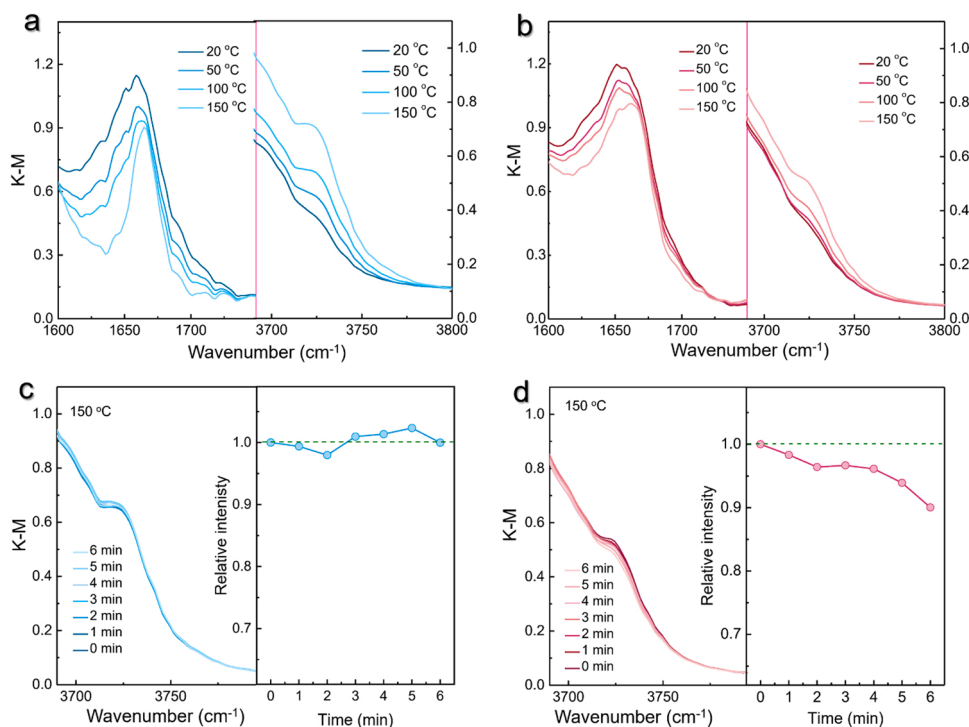


Fig. 5. *In-situ* DRIFTS spectra in the 1600–1750 cm^{-1} and 3690–3800 cm^{-1} range of H-O-H and -OH adsorption on the (a) PtK_x and (b) Pt nanoparticles at various temperatures, respectively. *In-situ* DRIFTS spectra in the 3690–3800 cm^{-1} range of -OH adsorption on the (c) PtK_x and (d) Pt nanoparticles at various times, when the temperature was fixed at 150 °C.

intermediates.

4. Conclusion

In conclusion, we have demonstrated a new and convenient strategy to improve H_2O dissociation and stabilize the generated $^*\text{OH}$ intermediate via the K^+ -doped Pt nanoparticles, thereby boosting the highly performed H_2 generation through APRM at low temperatures. At 120 °C, the K^+ -doped Pt nanoparticles anchored on Al_2O_3 yielded a TOF of 142.3 h^{-1} for H_2 generation in comparison with the no activity of Pt nanoparticles with similar size deposited on the identical support. More importantly, the K^+ -doped Pt catalysts effectively suppressed the CO generation ($<10 \text{ ppm}$), which satisfy the demands of the direct supply for the downstream applications without additional CO transformation system. Catalytic mechanism investigations revealed that the K^+ -enabled stability of $^*\text{OH}$ and then promoted reforming with the $^*\text{CO}$ intermediate on Pt nanoparticles as the critical factors enhanced the catalytic hydrogen generation of Pt through APRM pathway. This study provides a practical guidance of catalyst design for hydrogen production through APRM at low temperatures and promotes the possibility of large-scale application of hydrogen generation from steam reforming of methanol.

CRediT authorship contribution statement

You Wang performed most of the experiments and wrote the paper. **Bing Liu** carried out the DFT calculations. **Sai Zhang** and **Yongquan Qu** designed the studies, wrote, and revised the paper. All authors discussed the results and commented on the manuscript.

Declaration of Competing Interest

The authors declare that they have no competing interests.

Data Availability

Data will be made available on request.

Acknowledgments

We acknowledge the National Natural Science Foundation of China (22002115), the Guangdong Basic and Applied Basic Research Foundation (2022B1515020092), Shenzhen Science and Technology Program (JCYJ20220530161600002), and Key Research and Development Program of Shaanxi Province (2023-YBGY-299).

Appendix A. Supporting information

Supplementary data associated with this article can be found in the online version at [doi:10.1016/j.apcatb.2023.123011](https://doi.org/10.1016/j.apcatb.2023.123011).

References

- [1] K. Jiao, J. Xuan, Q. Du, Z. Bao, B. Xie, B. Wang, Y. Zhao, L. Fan, H. Wang, Z. Hou, S. Huo, N.P. Brandon, Y. Yin, M.D. Guiver, Designing the next generation of proton-exchange membrane fuel cells, *Nature* 595 (2021) 361–369, <https://doi.org/10.1038/s41586-021-03482-7>.
- [2] H.-Y. Do, C.-H. Kim, J.-Y. Han, H.-S. Kim, S.-K. Ryi, Low-temperature proton-exchange membrane fuel cell-grade hydrogen production by membrane reformer equipped with Pd-composite membrane and methanation catalyst on permeation stream, *J. Membr. Sci.* 634 (2021), 119373, <https://doi.org/10.1016/j.memsci.2021.119373>.
- [3] R. Haider, Y. Wen, Z.F. Ma, D.P. Wilkinson, L. Zhang, X. Yuan, S. Song, J. Zhang, High temperature proton exchange membrane fuel cells: progress in advanced materials and key technologies, *Chem. Soc. Rev.* 50 (2021) 1138–1187, <https://doi.org/10.1039/d0cs00296h>.
- [4] T. Asset, P. Atanassov, Iron-nitrogen-carbon catalysts for proton exchange membrane fuel cells, *Joule* 4 (2020) 33–44, <https://doi.org/10.1016/j.joule.2019.12.002>.
- [5] G. Gao, L.-W. Wang, A potential and pH inclusive microkinetic model for hydrogen reactions on Pt surface, *Chem. Catal.* 1 (2021) 1331–1345, <https://doi.org/10.1016/j.checat.2021.10.006>.
- [6] S.Z.A. Ghafri, S. Munro, U. Cardella, T. Funke, W. Notardonato, J.P.M. Trusler, J. Leachman, R. Span, S. Kamiya, G. Pearce, A. Swanger, E.D. Rodriguez, P. Bajada,

- F. Jiao, K. Peng, A. Siahvashi, M.L. Johns, E.F. May, Hydrogen liquefaction: a review of the fundamental physics, engineering practice and future opportunities, *Energy Environ. Sci.* 15 (2022) 2690–2731, <https://doi.org/10.1039/d2ee00099g>.
- [7] D. Teichmann, W. Arlt, P. Wasserscheid, R. Freymann, A future energy supply based on liquid organic hydrogen carriers (LOHC), *Energy Environ. Sci.* 4 (2011) 2767–2773, <https://doi.org/10.1039/c1ee01454d>.
- [8] H. Yu, Y. Wu, S. Chen, Z. Xie, Y. Wu, N. Cheng, X. Yang, W. Lin, L. Xie, X. Li, J. Zheng, Pd-modified LaNi₅ nanoparticles for efficient hydrogen storage in a carbazole type liquid organic hydrogen carrier, *Appl. Catal. B-Environ.* 317 (2022), 121720, <https://doi.org/10.1016/j.apcatb.2022.121720>.
- [9] K. Naveen, T. Mahvelati-Shamsabadi, P. Sharma, S.H. Lee, S.H. Hur, W.M. Choi, T. J. Shin, J.S. Chung, Co/Zn single-atom catalysts for reversible hydrogenation and dehydrogenation of quinoline hydrogen carrier, *Appl. Catal. B-Environ.* 328 (2023), 122482, <https://doi.org/10.1016/j.apcatb.2023.122482>.
- [10] C.-I. Ahn, Y. Kwak, A.-R. Kim, M. Jang, A. Badakhsh, J. Cha, Y. Kim, Y.S. Jo, H. Jeong, S.H. Choi, S.-R. Nam, C.W. Yoon, H. Sohn, Dehydrogenation of homocyclic liquid organic hydrogen carriers (LOHCs) over Pt supported on an ordered pore structure of 3-D cubic mesoporous KIT-6 silica, *Appl. Catal. B-Environ.* 307 (2022), 121169, <https://doi.org/10.1016/j.apcatb.2022.121169>.
- [11] M. Nielsen, E. Alberico, W. Baumann, H.J. Drexler, H. Junge, S. Gladioli, M. Beller, Low-temperature aqueous-phase methanol dehydrogenation to hydrogen and carbon dioxide, *Nature* 495 (2013) 85–89, <https://doi.org/10.1038/nature11891>.
- [12] L. Lin, W. Zhou, R. Gao, S. Yao, X. Zhang, W. Xu, S. Zheng, Z. Jiang, Q. Yu, Y.W. Li, C. Shi, X.D. Wen, D. Ma, Low-temperature hydrogen production from water and methanol using Pt/alpha-MoC catalysts, *Nature* 544 (2017) 80–83, <https://doi.org/10.1038/nature21672>.
- [13] Y. Wang, W. Gao, K. Li, Y. Zheng, Z. Xie, W. Na, J.G. Chen, H. Wang, Strong evidence of the role of H₂O in affecting methanol selectivity from CO₂ hydrogenation over Cu-ZnO-ZrO₂, *Chem* 6 (2020) 419–430, <https://doi.org/10.1016/j.chempr.2019.10.023>.
- [14] R.D. Cortright, R.R. Davda, J.A. Dumesic, Hydrogen from catalytic reforming of biomass-derived hydrocarbons in liquid water, *Nature* 418 (2002) 964–967, <https://doi.org/10.1038/nature01009>.
- [15] L. Lin, Q. Yu, M. Peng, A. Li, S. Yao, S. Tian, X. Liu, A. Li, Z. Jiang, R. Gao, X. Han, Y.W. Li, X.D. Wen, W. Zhou, D. Ma, Atomically dispersed Ni/alpha-MoC catalyst for hydrogen production from methanol/water, *J. Am. Chem. Soc.* 142 (2020) 309–317, <https://doi.org/10.1021/jacs.0c10776>.
- [16] D. Li, F. Xu, X. Tang, S. Dai, T. Pu, X. Liu, P. Tian, F. Xuan, Z. Xu, I.E. Wachs, M. Zhu, Induced activation of the commercial Cu/ZnO/Al₂O₃ catalyst for the steam reforming of methanol, *Nat. Catal.* 5 (2022) 99–108, <https://doi.org/10.1038/s41929-021-00729-4>.
- [17] A.M. Ranjekar, G.D. Yadav, Steam reforming of methanol for hydrogen production: a critical analysis of catalysis, processes, and scope, *Ind. Eng. Chem. Res.* 60 (2021) 89–113, <https://doi.org/10.1021/acs.iecr.0c05041>.
- [18] K. Fujita, R. Kawahara, T. Aikawa, R. Yamaguchi, Hydrogen production from a methanol-water solution catalyzed by an anionic iridium complex bearing a functional bipyridonate ligand under weakly basic conditions, *Angew. Chem. Int. Ed. Engl.* 54 (2015) 9057–9060, <https://doi.org/10.1002/anie.201502194>.
- [19] E. Alberico, A.J. Lennox, L.K. Vogt, H. Jiao, W. Baumann, H.J. Drexler, M. Nielsen, A. Spannenberg, M.P. Checinski, H. Junge, M. Beller, Unravelling the mechanism of basic aqueous methanol dehydrogenation catalyzed by Ru-PNP pincer complexes, *J. Am. Chem. Soc.* 138 (2016) 14890–14904, <https://doi.org/10.1021/jacs.6b05692>.
- [20] S. Zhang, Y. Ma, H. Zhang, X. Zhou, X. Chen, Y. Qu, Additive-free, robust H₂ production from H₂O and DMF by dehydrogenation catalyzed by Cu/Cu₂O formed in situ, *Angew. Chem. Int. Ed.* 56 (2017) 8245–8249, <https://doi.org/10.1002/anie.201704381>.
- [21] S. Zhang, Y. Liu, M. Zhang, Y. Ma, J. Hu, Y. Qu, Sustainable production of hydrogen with high purity from methanol and water at low temperatures, *Nat. Commun.* 13 (2022) 5527, <https://doi.org/10.1038/s41467-022-33186-z>.
- [22] L. Chen, Z. Qi, X. Peng, J.L. Chen, C.W. Pao, X. Zhang, C. Dun, M. Young, D. Prendergast, J.J. Urban, J. Guo, G.A. Somorjai, J. Su, Insights into the mechanism of methanol steam reforming tandem reaction over CeO₂ supported single-site catalysts, *J. Am. Chem. Soc.* 143 (2021) 12074–12081, <https://doi.org/10.1021/jacs.1c03895>.
- [23] Y. Zhai, D. Pierre, R. Si, W. Deng, P. Ferrin, A.U. Nilekar, G. Peng, J.A. Herron, D. C. Bell, H. Saltsburg, M. Mavrikakis, M. Flytzani-Stephanopoulos, Alkali-stabilized Pt-OHx species catalyze low-temperature water-gas shift reactions, *Science* 329 (2010) 1633–1636, <https://doi.org/10.1126/science.1192449>.
- [24] J.A. Rodriguez, S. Ma, P. Liu, J. Hrbek, J. Evans, M. Pérez, Activity of CeO_x and TiO_x nanoparticles grown on Au(111) in the water-gas shift reaction, *Science* 318 (2007) 1757–1760, <https://doi.org/10.1126/science.1150038>.
- [25] J.G. Chen, Tuning catalytic properties using an atomically dispersed metal overlayer on transition metal carbide substrates, *Natl. Sci. Rev.* 4 (2017) 788–789, <https://doi.org/10.1093/nsr/nwx090>.
- [26] L.N. Chen, K.P. Hou, Y.S. Liu, Z.Y. Qi, Q. Zheng, Y.H. Lu, J.Y. Chen, J.L. Chen, C. W. Pao, S.B. Wang, Y.B. Li, S.H. Xie, F.D. Liu, D. Prendergast, L.E. Klebanoff, V. Stavila, M.D. Allendorf, J. Guo, L.S. Zheng, J. Su, G.A. Somorjai, Efficient hydrogen production from methanol using a single-site Pt₁/CeO₂ catalyst, *J. Am. Chem. Soc.* 141 (2019) 17995–17999, <https://doi.org/10.1021/jacs.9b09431>.
- [27] J. Greeley, M. Mavrikakis, A first-principles study of methanol decomposition on Pt (111), *J. Am. Chem. Soc.* 124 (2002) 7193–7201, <https://doi.org/10.1021/ja017818k>.
- [28] J. Greeley, M. Mavrikakis, Competitive paths for methanol decomposition on Pt (111), *J. Am. Chem. Soc.* 126 (2004) 3910–3919, <https://doi.org/10.1021/ja037700z>.
- [29] A.J. Therrien, K. Groden, A.J.R. Hensley, A.C. Schilling, R.T. Hannagan, M. D. Marcinkowski, A. Pronschinske, F.R. Lucci, E.C.H. Sykes, J.-S. McEwen, Water activation by single Pt atoms supported on a Cu₂O thin film, *J. Catal.* 364 (2018) 166–173, <https://doi.org/10.1016/j.jcat.2018.04.024>.
- [30] R. Subbaraman, D. Tripkovic, D. Strmcnik, K.-C. Chang, M. Uchimura, A. P. Paulikas, V. Stamenkovic, N.M. Markovic, Enhancing hydrogen evolution activity in water splitting by tailoring Li⁺-Ni(OH)₂-Pt interfaces, *Science* 334 (2011) 1256–1260, <https://doi.org/10.1126/science.1211934>.
- [31] Y. Ishikawa, M.-S. Liao, C.R. Cabrera, Energetics of H₂O dissociation and CO_{ads} + OH_{ads} reaction on a series of Pt-M mixed metal clusters: a relativistic density-functional study, *Surf. Sci.* 513 (2002) 98–110, [https://doi.org/10.1016/S0039-6028\(02\)01697-7](https://doi.org/10.1016/S0039-6028(02)01697-7).
- [32] Q. Wang, J. Lan, R. Liang, Y. Xia, L. Qin, L.W. Chung, Z. Zheng, New tricks for an old dog: Grubbs catalysts enable efficient hydrogen production from aqueous-phase methanol reforming, *ACS Catal.* 12 (2022) 2212–2222, <https://doi.org/10.1021/acscatal.1c05369>.
- [33] R.E. Rodriguez-Lugo, M. Trincado, M. Vogt, F. Tewes, G. Santiso-Quinones, H. Grutzmacher, A homogeneous transition metal complex for clean hydrogen production from methanol-water mixtures, *Nat. Chem.* 5 (2013) 342–347, <https://doi.org/10.1038/nchem.1595>.
- [34] K. Ding, A. Gulec, A.M. Johnson, N.M. Schweitzer, G.D. Stucky, L.D. Marks, P. C. Stair, Identification of active sites in CO oxidation and water-gas shift over supported Pt catalysts, *Science* 350 (2015) 189–192, <https://doi.org/10.1126/science.1263688>.
- [35] M. Flytzani-Stephanopoulos, Gold atoms stabilized on various supports catalyze the water-gas shift reaction, *Acc. Chem. Res.* 47 (2013) 783–792, <https://doi.org/10.1021/ar4001845>.
- [36] E.M. Karp, T.L. Silbaugh, M.C. Crowe, C.T. Campbell, Energetics of adsorbed methanol and methoxy on Pt(111) by microcalorimetry, *J. Am. Chem. Soc.* 134 (2012) 20388–20395, <https://doi.org/10.1021/ja307465u>.
- [37] R. Garcia-Muelas, Q. Li, N. López, Density functional theory comparison of methanol decomposition and reverse reactions on metal surfaces, *ACS Catal.* 5 (2015) 1027–1036, <https://doi.org/10.1021/cs501698w>.
- [38] X.-K. Gu, W.-X. Li, First-principles study on the origin of the different selectivities for methanol steam reforming on Cu(111) and Pd(111), *J. Phys. Chem. C* 114 (2010) 21539–21547, <https://doi.org/10.1021/jp107678d>.
- [39] Z.-J. Zhao, S. Liu, S. Zha, D. Cheng, F. Studt, G. Henkelman, J. Gong, Theory-guided design of catalytic materials using scaling relationships and reactivity descriptors, *Nat. Rev. Mater.* 4 (2019) 792–804, <https://doi.org/10.1038/s41578-019-0152-x>.
- [40] Y. Li, Y. Sun, Y. Qin, W. Zhang, L. Wang, M. Luo, H. Yang, S. Guo, Recent advances on water-splitting electrocatalysis mediated by noble-metal-based nanostructured materials, *Adv. Energ. Mater.* 10 (2020), <https://doi.org/10.1002/aenm.201903120>.
- [41] X. Wang, Y. Zheng, W. Sheng, Z.J. Xu, M. Jaroniec, S.-Z. Qiao, Strategies for design of electrocatalysts for hydrogen evolution under alkaline conditions, *Mater. Today* 36 (2020) 125–138, <https://doi.org/10.1016/j.mattod.2019.12.003>.
- [42] A. Michaelides, P. Hu, Catalytic water formation on platinum: a first-principles study, *J. Am. Chem. Soc.* 123 (2001) 4235–4242, <https://doi.org/10.1021/ja003576x>.
- [43] A.A. Phatak, W.N. Delgass, F.H. Ribeiro, W.F. Schneider, Density functional theory comparison of water dissociation steps on Cu, Au, Ni, Pd, and Pt, *J. Phys. Chem. C* 113 (2009) 7269–7276, <https://doi.org/10.1021/jp810216b>.
- [44] M. Hamed, T. Watanabe, N. Kamiuchi, M. Ozawa, Effect of platinum dispersion on the catalytic activity of Pt/Al₂O₃ for the oxidation of carbon monoxide and propene, *Appl. Catal. B-Environ.* 142–143 (2013) 8–14, <https://doi.org/10.1016/j.apcatb.2013.04.055>.
- [45] J.A. Anderson, R.A. Daley, S.Y. Christou, A.M. Efstathiou, Regeneration of thermally aged Pt-Rh/Ce_xZr_{1-x}O₂-Al₂O₃ model three-way catalysts by oxychlorination treatments, *Appl. Catal. B-Environ.* 64 (2006) 189–200, <https://doi.org/10.1016/j.apcatb.2005.12.007>.
- [46] K. Fujita, R. Kawahara, T. Aikawa, R. Yamaguchi, Hydrogen production from a methanol-water solution catalyzed by an anionic iridium complex bearing a functional bipyridonate ligand under weakly basic conditions, *Angew. Chem. Int. Ed.* 54 (2015) 9057–9060, <https://doi.org/10.1002/anie.201502194>.
- [47] P. Hu, Y. Diskin-Posner, Y. Ben-David, D. Milstein, Reusable homogeneous catalytic system for hydrogen production from methanol and water, *ACS Catal.* 4 (2014) 2649–2652, <https://doi.org/10.1021/cs500937f>.
- [48] J. Luo, S. Kar, M. Rauch, M. Montag, Y. Ben-David, D. Milstein, Efficient base-free aqueous reforming of methanol homogeneously catalyzed by ruthenium exhibiting a remarkable acceleration by added catalytic thiol, *J. Am. Chem. Soc.* 143 (2021) 17284–17291, <https://doi.org/10.1021/jacs.1c09007>.
- [49] Y. Shi, J. Li, D. Huang, X. Wang, Y. Huang, C. Chen, R. Li, Specific adsorption and efficient degradation of cylindrospermopsin on oxygen-vacancy sites of BiOBr, *ACS Catal.* 13 (2022) 445–458, <https://doi.org/10.1021/acscatal.2c04228>.
- [50] X. Song, C. Yang, X. Li, Z. Wang, C. Pei, Z.-J. Zhao, J. Gong, On the role of hydroxyl groups on Cu/Al₂O₃ in CO₂ hydrogenation, *ACS Catal.* 12 (2022) 14162–14172, <https://doi.org/10.1021/acscatal.2c03591>.
- [51] J. Saavedra, C.J. Pursell, B.D. Chandler, CO oxidation kinetics over Au/TiO₂ and Au/Al₂O₃ catalysts: evidence for a common water-assisted mechanism, *J. Am. Chem. Soc.* 140 (2018) 3712–3723, <https://doi.org/10.1021/jacs.7b12758>.
- [52] N. Acerbi, S.C. Tsang, G. Jones, S. Golunski, P. Collier, Rationalization of interactions in precious metal/ceria catalysts using the d-band center model,

- Angew. Chem. Int. Ed. 52 (2013) 7737–7741, <https://doi.org/10.1002/anie.201300130>.
- [53] B. Hammer, J.K. Nørskov, Electronic factors determining the reactivity of metal surfaces, *Surf. Sci.* 343 (1995) 211–220, [https://doi.org/10.1016/0039-6028\(96\)00588-2](https://doi.org/10.1016/0039-6028(96)00588-2).
- [54] J.R. Kitchin, J.K. Nørskov, M.A. Barteau, J.G. Chen, Modification of the surface electronic and chemical properties of Pt(111) by subsurface 3d transition metals, *J. Chem. Phys.* 120 (2004) 10240–10246, <https://doi.org/10.1063/1.1737365>.